



Visualization of three-dimensional incompressible flows by quasi-two-dimensional divergence-free projections



Alexander Yu. Gelfgat *

School of Mechanical Engineering, Faculty of Engineering, Tel-Aviv University, Ramat Aviv, Tel-Aviv 69978, Israel

ARTICLE INFO

Article history:

Received 8 April 2013

Received in revised form 2 April 2014

Accepted 4 April 2014

Available online 16 April 2014

Keywords:

Incompressible flow

Flow visualization

Galerkin method

Natural convection benchmark

Lid-driven cavity benchmark

ABSTRACT

Context: A visualization of three-dimensional incompressible flows by divergence-free quasi-two-dimensional projections of velocity field on three coordinate planes is proposed.

Objective: To visualize 3D incompressible flow by 3 two-dimensional plots.

Method: It is argued that such divergence-free projections satisfying all the velocity boundary conditions are unique for a given velocity field. It is shown that the projected fields and their vector potentials can be calculated using divergence-free Galerkin bases.

Results: Using natural convection flow in a laterally heated cube as an example, it is shown that the projections proposed allow for a better understanding of similarities and differences of three-dimensional flows and their two-dimensional likenesses. An arbitrary choice of projection planes is further illustrated by a lid-driven flow in a cube, where the lid moves parallel either to a sidewall or a diagonal plane.

Conclusion: A new method for visualization of 3D incompressible flows is developed and described.

© 2014 Elsevier Ltd. All rights reserved.

1. Introduction

With the growth of available computer power, development of numerical methods and experimental techniques dealing with fully developed three-dimensional flows the importance of flow visualization becomes obvious. While two-dimensional flows can be easily described by streamline or vector plots, there is no commonly accepted methodology for representation of three-dimensional flows on a 2D plot. Streamlines can be defined also for a general 3D flow, however cannot be represented by a single stream function. Other textbook techniques, such as streak lines, trajectories and arrow fields, are widely used but become unhelpful with increase of flow complexity. Same can be said about plotting of iso-surfaces and isolines of velocity or vorticity components, which produce beautiful pictures, however, do not allow one to find out velocity direction at a certain point. Basic and more advanced recent state-of-the-art visualization techniques are discussed in review papers [1–3] where reader is referred for the details. Here we develop another visualization technique, applicable only to incompressible flows, and related to the surface-based techniques discussed in [2]. Our technique considers projections of 3D velocity field onto coordinate planes and allows one to compute a set of surfaces to which the projected flow is tangent. Thus, the flow is visualized in all three sets of coordinate planes (surfaces). The

choice of visualization coordinate system is arbitrary, so that the axes can be directed along “most interesting” directions, e.g. directions parallel and orthogonal to dominating velocity or vorticity.

The goal of this study is to visualize a three-dimensional incompressible flow computed numerically at some grid nodes. The visualization described below is independent on the method used for flow calculation. It is based on divergence-free projections of a computed 3D velocity field on two-dimensional coordinate planes. Initially, this study was motivated by a need to visualize three-dimensional benchmark flows, which are direct extensions of well-known two-dimensional benchmarks, e.g., lid-driven cavity and convection in laterally heated rectangular cavities. Thus, we seek for a visualization that is capable to show clearly both similarities and differences of flows considered in 2D and 3D formulations. It seems, however, that the technique proposed can have significantly wider area of applications and can be applied for visualization of different divergence free vector functions, e.g., vorticity and magnetic field. The last example below illustrates that the technique allows one to visualize along or perpendicular to an arbitrarily chosen direction that can differ from coordinate axes.

Consider a given velocity field, which can be a result of computation or experimental measurement. Note, that modern means of flow measurement, like PIV and PTV, allow one to measure three velocity components on quite representative grids, which leads to the same problem of visualization of results. Here we observe that a three-dimensional divergence-free velocity field can be represented as a superposition of two vector fields that describe the

* Tel.: +972 36407207; fax: +972 36407334.

E-mail address: gelfgat@tau.ac.il

motion in two sets of coordinate planes, say $(x-z)$ and $(y-z)$, without a need to consider the $(x-y)$ planes. These fields allow for definition of vector potential of velocity, whose two independent components have properties of two-dimensional stream function. The two parts of velocity field are tangent to isosurfaces of the vector potential components, which allows one to visualize the flow in two sets of orthogonal coordinate planes. This approach, however, does not allow one to preserve the velocity boundary conditions in each of the fields separately, so that some of the boundary conditions are satisfied only after both fields are superimposed. The latter is not good for visualization purposes. We argue further, that it is possible to define divergence-free projections of the flow on the three sets of coordinate planes, so that (i) the projections are unique, (ii) each projection is described by a single component of its vector potential, and (iii) the projection vectors are tangent to isosurfaces of the corresponding non-zero vector potential component. This allows us to visualize the flow in three orthogonal sets of coordinate planes. In particular, it helps to understand how the three-dimensional model flows differ from their two-dimensional likenesses. To calculate the projections we propose to use divergence-free Galerkin bases, on which the initial flow can be orthogonally projected. Clearly, these projections can be calculated by other numerical approaches.

For a representative example, we choose convection in a laterally heated square cavity with perfectly thermally insulated horizontal boundaries, and the corresponding three-dimensional extension, i.e., convection in a laterally heated cube with perfectly insulated horizontal and spanwise boundaries. The most representative solutions for steady states in these model flows can be found in [4] for the 2D benchmark, and in [5,6] for the 3D one. In these benchmarks the pressure p , velocity $\mathbf{v} = (u, v, w)$ and temperature T are obtained as a solution of Boussinesq equations

$$\frac{\partial T}{\partial t} + (\mathbf{v} \cdot \nabla) T = \Delta T \quad (1)$$

$$\frac{\partial \mathbf{v}}{\partial t} + (\mathbf{v} \cdot \nabla) \mathbf{v} = -\nabla p + Pr \Delta \mathbf{v} + Ra Pr T \mathbf{e}_z \quad (2)$$

$$\text{div}[\mathbf{v}] = 0 \quad (3)$$

defined in a square $0 \leq x, z \leq 1$ or in a cube $0 \leq x, y, z \leq 1$, with the no-slip boundary conditions on all the boundaries. The boundaries $x=0, 1$ are isothermal and all the other boundaries are thermally insulated, which in the dimensionless formulation reads

$$T(x=0) = 1, \quad T(x=1) = 0, \quad \left(\frac{\partial T}{\partial y}\right)_{y=0,1} = 0, \quad \left(\frac{\partial T}{\partial z}\right)_{z=0,1} = 0. \quad (4)$$

Ra and Pr are the Rayleigh and Prandtl numbers. The reader is referred to the above cited papers for more details. Here we focus only on visualization of solutions of 3D problem and comparison with the corresponding 2D flows. All the flows reported below are calculated on 100^2 and 100^3 stretched finite volume grids, which is accurate enough for present visualization purposes (for convergence studies see also [7]).

Apparently, the 2D flow $\mathbf{v} = (u, 0, w)$ is best visualized by the streamlines, which are the isolines of the stream function ψ defined as $u = \frac{\partial \psi}{\partial z}$, $w = -\frac{\partial \psi}{\partial x}$. In each point the velocity vector is tangent to a streamline passing through the same point, so that plot of streamlines and schematic indication of the flow direction is sufficient to visualize a two-dimensional flow. This is illustrated in Fig. 1, where streamlines of flows calculated for $Pr = 0.71$, and Ra varied from 10^3 to 10^8 are shown. Note how the streamline patterns get more complex with the increase of Rayleigh number. Our further purpose is to visualize three-dimensional flows at

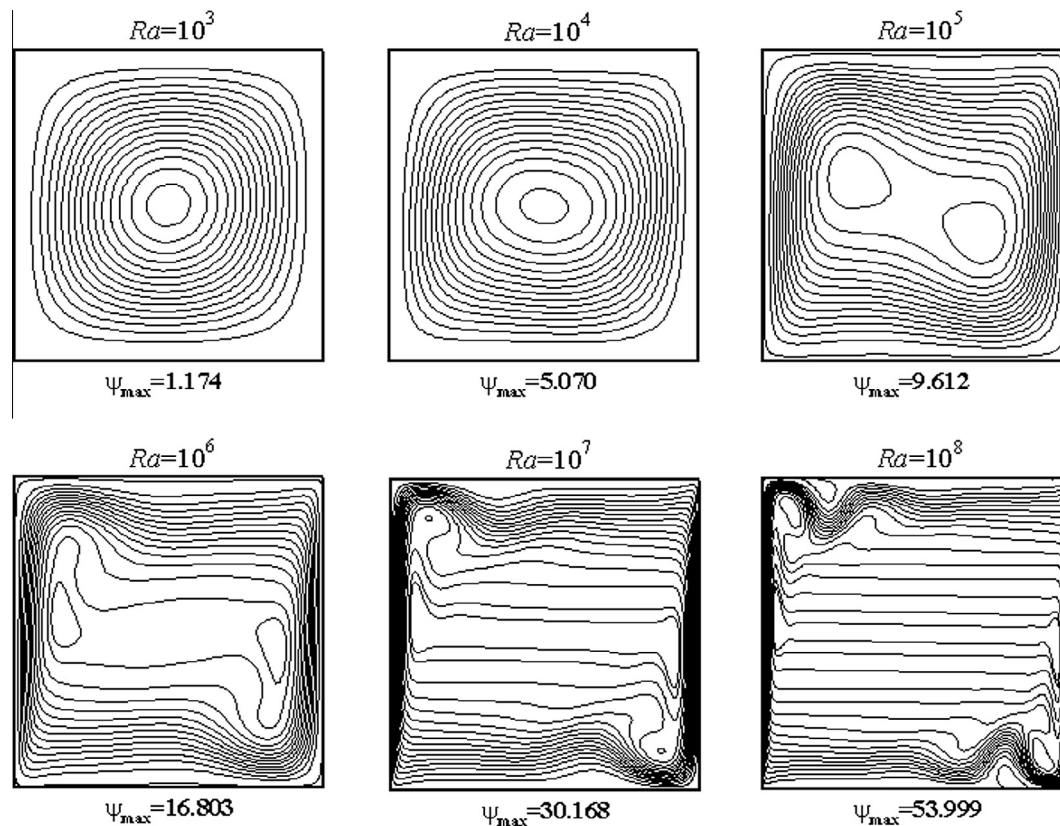


Fig. 1. Streamlines of two-dimensional buoyancy convection flow in a laterally heated square cavity at $Pr = 0.71$ and different Rayleigh numbers. The direction of main circulation is clockwise.

the same Rayleigh numbers, so that it will be possible to see similarities and differences between 2D and 3D flows.

2. Preliminary considerations

We consider an incompressible flow in a rectangular box $0 \leq x \leq X, 0 \leq y \leq Y, 0 \leq z \leq Z$, satisfying the no-slip conditions on all boundaries. The continuity equation $\partial u/\partial x + \partial v/\partial y + \partial w/\partial z = 0$ makes one velocity component dependent on two others, so that to describe the velocity field we need two scalar three-dimensional functions, while the third one can be found via continuity. This observation allows us to decompose the velocity field in the following way

$$\mathbf{v} = \begin{bmatrix} u \\ v \\ w \end{bmatrix} = \begin{bmatrix} u \\ 0 \\ w_1 \end{bmatrix} + \begin{bmatrix} 0 \\ v \\ w_2 \end{bmatrix}, \quad w_1 = -\int_0^z \frac{\partial u}{\partial x} dz, \quad w_2 = -\int_0^z \frac{\partial v}{\partial y} dz \tag{5}$$

This decomposition shows that the divergence-free velocity field can be represented as superposition of two fields having components only in the (x,z) or (y,z) planes. Moreover, we can easily define the vector potential of velocity field as

$$\Psi = \begin{bmatrix} \Psi_x \\ \Psi_y \\ 0 \end{bmatrix} = \begin{bmatrix} \int_0^z v dz \\ -\int_0^z u dz \\ 0 \end{bmatrix}, \quad \mathbf{v} = \text{rot}[\Psi] \tag{6}$$

Thus, Ψ is the vector potential of velocity field v , and its two non-zero components have properties of the stream function:

$$u = -\frac{\partial \Psi_y}{\partial z}, \quad w_1 = \frac{\partial \Psi_y}{\partial x}; \quad v = \frac{\partial \Psi_x}{\partial z}, \quad w_2 = -\frac{\partial \Psi_x}{\partial y}. \tag{7}$$

This means, in particular, that vectors of the two components of decomposition (5), i.e., $(u, 0, w_1)$ and $(0, v, w_2)$, are tangent to isosurfaces of Ψ_y and Ψ_x , and the vectors are located in the planes $(x-z)$ and $(y-z)$, respectively. Thus, it seems that the isosurfaces of Ψ_y and Ψ_x , which can be easily calculated from numerical or experimental (e.g., PIV) data, can be a good means for visualization of the velocity field. Unfortunately, there is a drawback, which can make such visualization meaningless. Namely, only the sum of vectors w_1 and w_2 , calculated via the integrals in (5), vanish at $z = Z$, while each vector separately does not. Thus, visualization of flow via the decomposition (5) in a straight-forward way will result in two fields that violate no-penetration boundary conditions at one of the boundaries, which would make the whole result quite meaningless. The latter is illustrated in Fig. 2, where isosurfaces of the two components of vector potentials are superimposed with the $(u, 0, w_1)$ and $(0, v, w_2)$ vectors. It is clearly seen that the vector arrows are tangent to the isosurfaces, however the velocities w_1 and w_2 do not vanish at the upper boundary. The latter is illustrated additionally by isolines of w_1 and w_2 plotted at the upper boundary (Fig. 2c and d). One can see also that the sum of functions plotted in Fig. 2c and d yields zero. Furthermore, the choice of integration boundaries in (5) is arbitrary, so that the whole decomposition (5) is not unique.

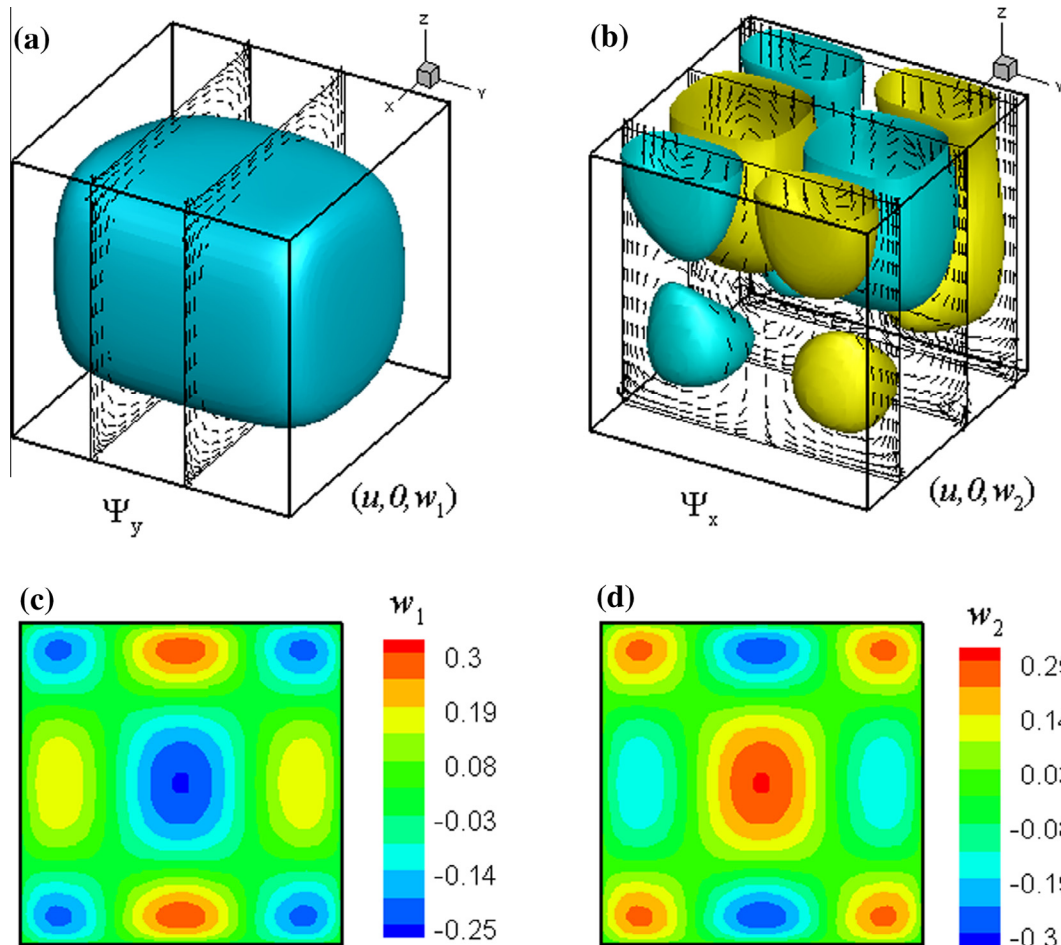


Fig. 2. Calculation for $Ra = 10^3$. Vector potentials Ψ_y and Ψ_x defined in Eq. (6) superposed with the vector fields $(u, 0, w_1)$ and $(0, v, w_2)$. (a) $\max \Psi_y = 1.066$, $\min \Psi_y = 0$, isosurface for $\Psi_y = 0.16$; (b) $\max |\Psi_x| = 0.053$, isosurfaces for $\Psi_x = \pm 0.008$. Frames (c) and (d) show isolines of the vectors w_1 and w_2 defined in Eq. (5) on the boundary $z = 1$.

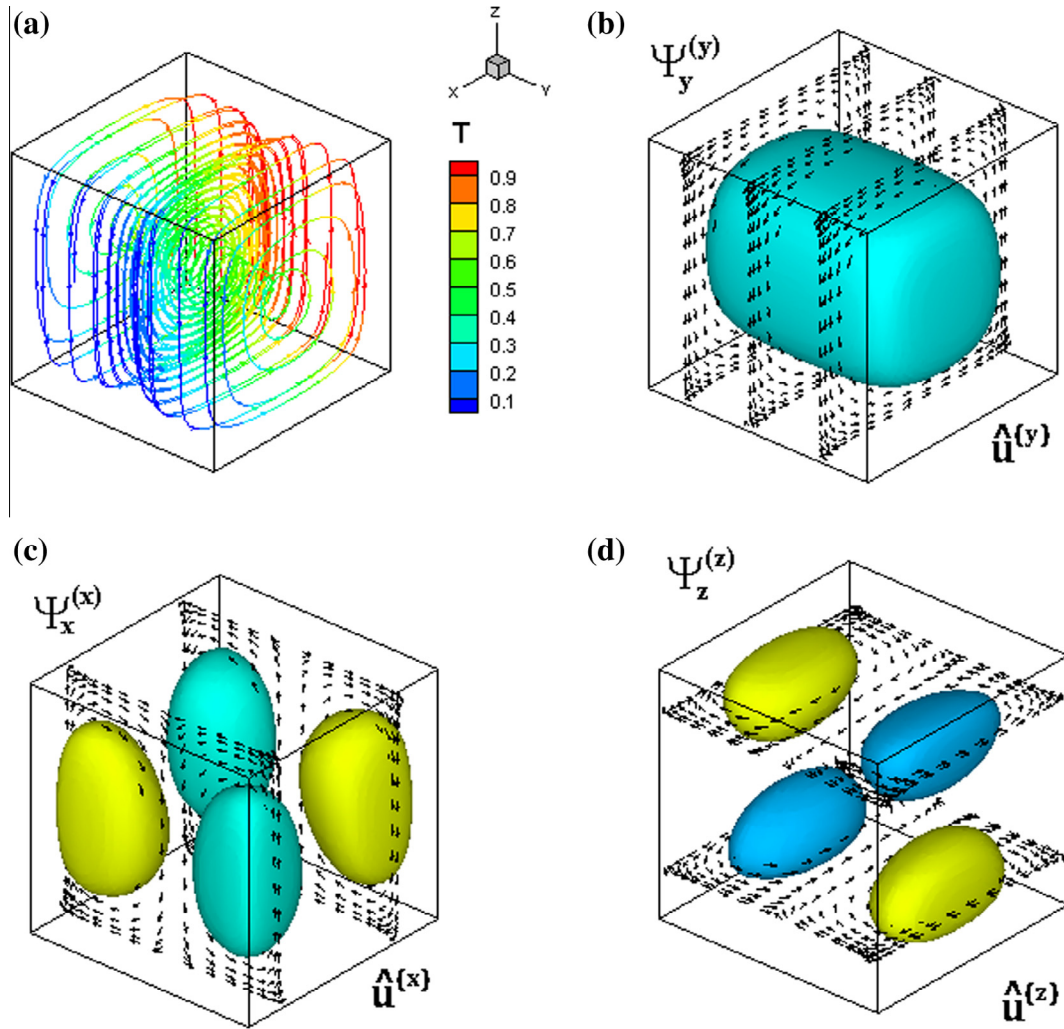


Fig. 3. Visualization of a three-dimensional flow at $Ra = 10^3$. (a) Two flow trajectories starting at the points $(0.1, 0.1, 0.1)$ and $(0.9, 0.9, 0.9)$. The trajectories are colored due to the temperature values at the points they pass. The temperature color map is shown aside. (b), (c), (d) Isosurfaces of $\Psi_y^{(y)}$, $\Psi_x^{(x)}$ and $\Psi_z^{(z)}$ superimposed with the vector plots of the fields $\hat{\mathbf{u}}^{(y)}$, $\hat{\mathbf{u}}^{(x)}$ and $\hat{\mathbf{u}}^{(z)}$, respectively. The isosurfaces are plotted for $\Psi_y^{(y)} = 0.28$, $\Psi_x^{(x)} = \pm 0.063$, and $\Psi_z^{(z)} = \pm 0.080$. (For interpretation of the references to color in this figure legend, the reader is referred to the web version of this article.)

Clearly, one would prefer to visualize unique properties of the flow rather than non-unique ones.

To define unique flow properties similar to those shown in Fig. 2 we observe that decomposition (5) can be interpreted as representation of a three-dimensional divergence-free vector into two divergence free vector fields located in orthogonal coordinate planes, i.e., having only two non-zero components. Consider a vector built from only two components of the initial field, say $\mathbf{u} = (u, v, 0)$. It is located in the $(x, y, z = \text{const})$ planes, satisfies all the boundary conditions for u and v , however, is not divergence-free. We can apply the Helmholtz–Leray decomposition [8] that decomposes this vector into solenoidal and potential part,

$$\mathbf{u} = \nabla\varphi + \hat{\mathbf{u}}, \quad \nabla \cdot \hat{\mathbf{u}} = 0 \quad (8)$$

As is shown in [8], together with the boundary conditions

$$\hat{\mathbf{u}} \cdot \mathbf{n} = 0, \quad \text{and} \quad \frac{\partial\varphi}{\partial n} = \mathbf{u} \cdot \mathbf{n} \quad (9)$$

where \mathbf{n} is a normal to the boundary, the decomposition (8) is unique. For the following, we consider (8) in the $(x, y, z = \text{const})$ planes and seek for a decomposition of $\mathbf{u} = (u, v, 0)$ in a $(x, y, z = \text{const})$ plane

$$\mathbf{u} = \nabla_{(x,y)}\varphi + \hat{\mathbf{u}}, \quad \nabla_{(x,y)} \cdot \hat{\mathbf{u}} = 0, \quad \nabla_{(x,y)} = \mathbf{e}_x \frac{\partial}{\partial x} + \mathbf{e}_y \frac{\partial}{\partial y}. \quad (10)$$

Table 1

Maximal values of the calculated vector potentials of the three velocity projections and their locations.

Ra	10^3	10^4	10^5	10^6	10^7	10^8
$\Psi_x^{(x)}$	0.144	0.602	1.408	2.925	5.988	15.200
x_{max}	0.812	0.867	0.926	0.956	0.0272	0.176
y_{max}	0.159	0.118	0.0702	0.0419	0.0969	0.0921
z_{max}	0.465	0.414	0.364	0.315	0.745	0.877
$\Psi_y^{(y)}$	1.127	4.993	9.954	17.863	32.854	61.465
x_{max}	0.509	0.509	0.693	0.841	0.0844	0.0521
y_{max}	0.500	0.653	0.812	0.912	0.0444	0.0236
z_{max}	0.500	0.483	0.414	0.431	0.535	0.535
$\Psi_z^{(z)}$	0.148	0.768	1.915	3.983	14.793	33.272
x_{max}	0.517	0.586	0.535	0.154	0.133	0.960
y_{max}	0.154	0.154	0.143	0.176	0.176	0.980
z_{max}	0.805	0.805	0.841	0.936	0.963	0.254

We represent the divergence-free two-dimensional vector $\hat{\mathbf{u}} = (\hat{u}, \hat{v}, 0)$ as

$$\hat{\mathbf{u}} = \text{rot}[\Psi], \quad \Psi = (0, 0, \Psi_z) \Rightarrow \hat{u} = \frac{\partial\Psi_z}{\partial y}, \quad \hat{v} = -\frac{\partial\Psi_z}{\partial x} \quad (11)$$

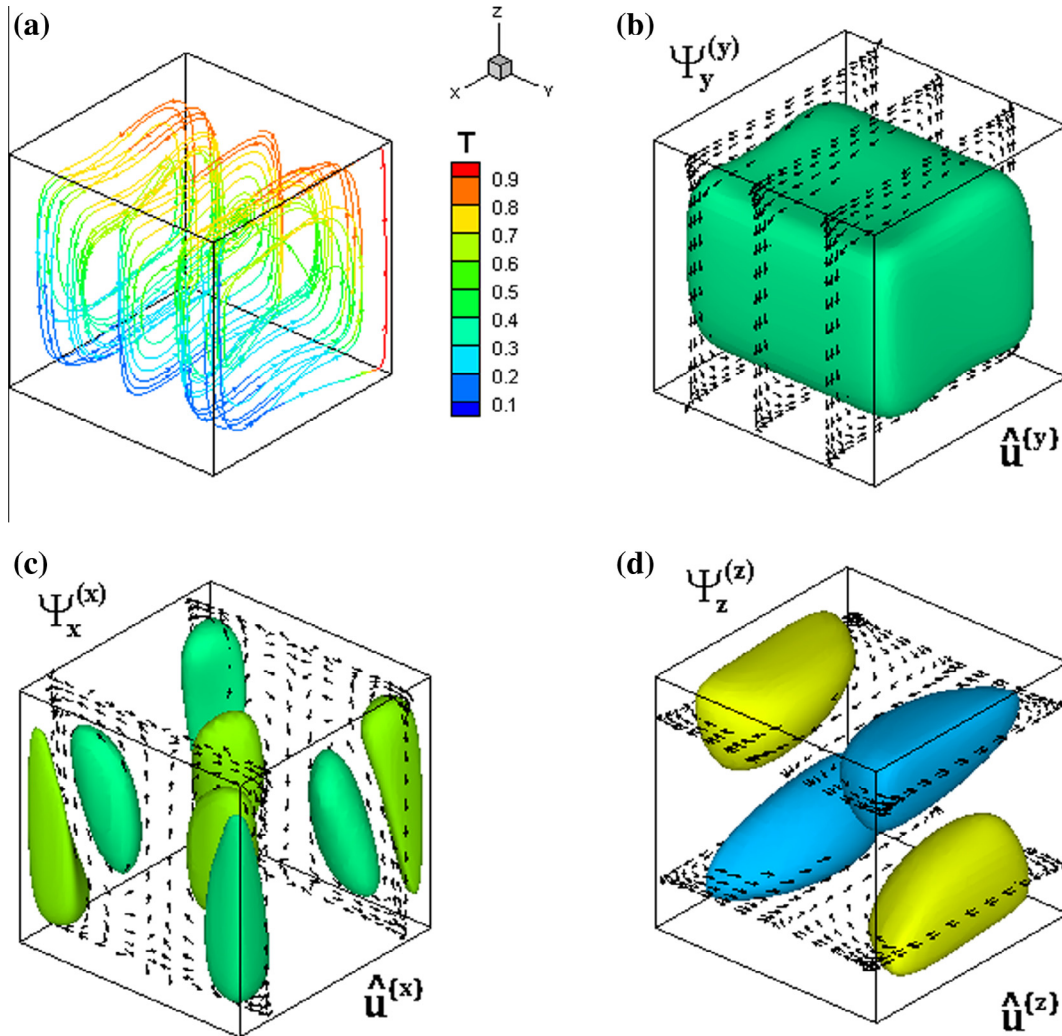


Fig. 4. Visualization of a three-dimensional flow at $Ra = 10^5$. (a) Two flow trajectories starting at the points $(0.1, 0.1, 0.1)$ $(0.9, 0.9, 0.9)$ and $(0.4, 0.5, 0.5)$. The trajectories are colored due to the temperature values at the points they pass. The temperature color map is shown aside. (b), (c), (d) Isosurfaces of Ψ_y , Ψ_x and Ψ_z superimposed with the vector plots of the fields $\hat{\mathbf{u}}^{(y)}$, $\hat{\mathbf{u}}^{(x)}$ and $\hat{\mathbf{u}}^{(z)}$, respectively. The isosurfaces are plotted for $\Psi_y = 4.0$, $\Psi_x = \pm 0.46$, and $\Psi_z = \pm 0.8$. (For interpretation of the references to color in this figure legend, the reader is referred to the web version of this article.)

which yields for the z-component of $rot[\mathbf{u}]$:

$$\mathbf{e}_z \cdot rot[\mathbf{u}] = \mathbf{e}_z \cdot rot[\hat{\mathbf{u}}] = \mathbf{e}_z \cdot rot[rot[\Psi]] = -\mathbf{e}_z \cdot \Delta \Psi = -\Delta \Psi_z \quad (12)$$

This shows that Ψ_z is an analog of the two-dimensional stream function, so that in each plane $(x, y, z = const)$ vector $\hat{\mathbf{u}}$ is tangent to an isoline of Ψ_z . To satisfy the no-slip boundary conditions for $\hat{\mathbf{u}}$ and \hat{v} , Ψ_z and its normal derivative must vanish on the boundary, which makes the definition of both Ψ_z and $\hat{\mathbf{u}}$ unique. Note, that contrary to the boundary conditions (9), to make vector $\hat{\mathbf{u}}$ in the decomposition (10) unique and satisfying all the boundary conditions of \mathbf{u} , we do not need to define any boundary conditions for the scalar potential φ .

To conclude, the resulting solenoidal part $\hat{\mathbf{u}}$ of vector $\mathbf{u} = (u, v, 0)$ (i) is unique, (ii) is defined by a single non-zero z-component Ψ_z of its vector potential, and (iii) in each $(x, y, z = const)$ plane vectors of $\hat{\mathbf{u}}$ are tangent to the isosurfaces of Ψ_z . Defining same solenoidal fields for two other sets of coordinate planes we arrive to three quasi-two-dimensional divergence-free projections of the initial velocity field. Each projection is described by a single scalar three-dimensional function, which, in fact, is a single non-zero component of the corresponding vector potential.

In the following we use the three above quasi-two-dimensional divergence-free projections for visualization of convective flow in a laterally heated cube, and offer a way to calculate them. In particular, to compare a three-dimensional result with the corresponding two-dimensional one, we need to compare one of the projections. Thus, if the 2D convective flow was considered in the plane (x, z) , we compare it with the corresponding projections of the 3D flow on the $(x, y = const, z)$ planes, which are tangent to isosurfaces of the non-zero y-component of the corresponding vector potential.

3. Numerical realization

A direct numerical implementation of the Helmholtz–Leray decomposition to an arbitrary velocity field is known in CFD as Chorin projection. This procedure is well-known, uses the boundary conditions (9), but does not preserve all the velocity boundary conditions. Therefore, it is not applicable for our purposes. Alternatively, we propose orthogonal projections of the initial velocity field on divergence-free Galerkin bases used previously for computations of different two-dimensional flows.

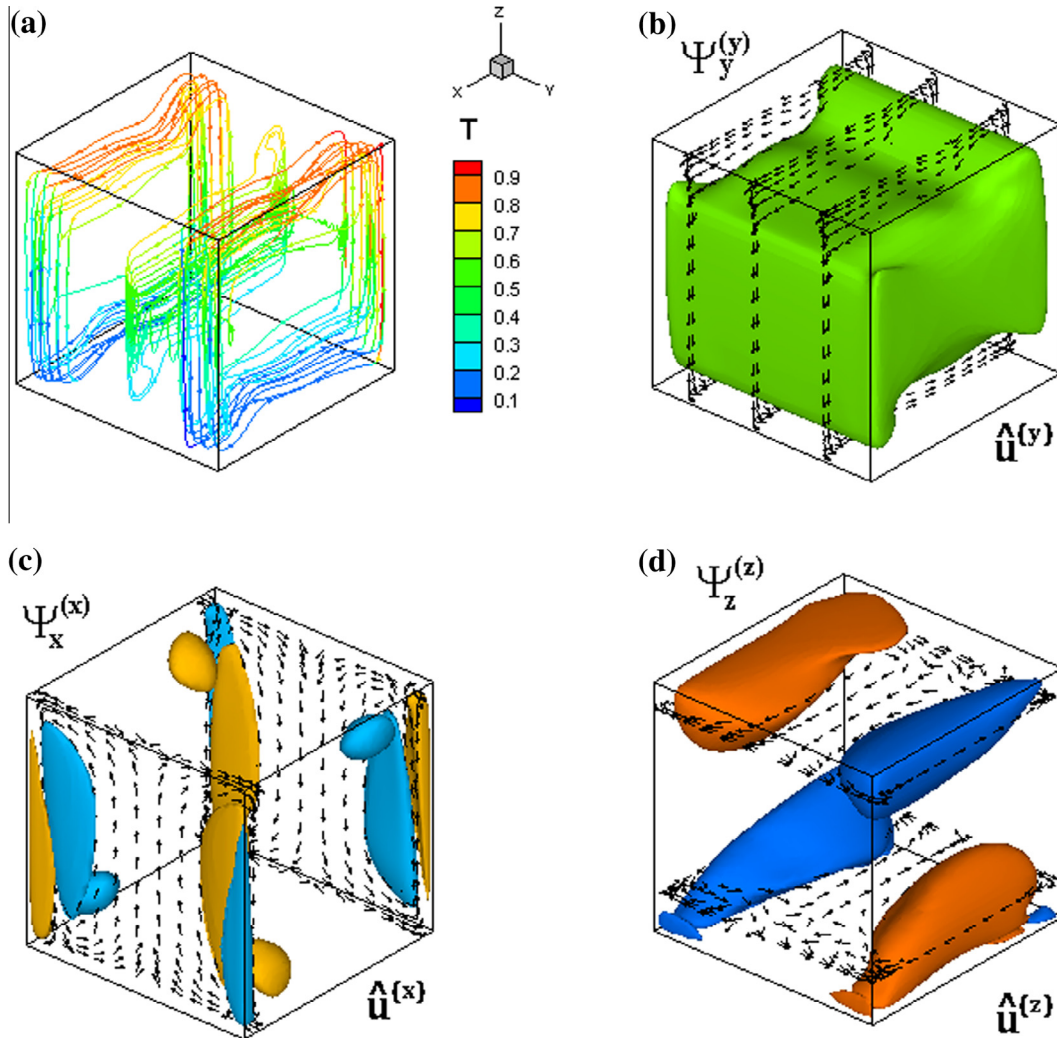


Fig. 5. Visualization of a three-dimensional flow at $Ra = 10^7$. (a) Two flow trajectories starting at the points $(0.1, 0.1, 0.1)$, $(0.9, 0.9, 0.9)$ and $(0.1, 0.5, 0.5)$. The trajectories are colored due to the temperature values at the points they pass. The temperature color map is shown aside. (b), (c), (d) Isosurfaces of $\Psi_y^{(y)}$, $\Psi_x^{(x)}$ and $\Psi_z^{(z)}$ superimposed with the vector plots of the fields $\mathbf{u}^{(y)}$, $\mathbf{u}^{(x)}$ and $\mathbf{u}^{(z)}$, respectively. The isosurfaces are plotted for $\Psi_y^{(y)} = 20.2$, $\Psi_x^{(x)} = \pm 1.94$, and $\Psi_z^{(z)} = \pm 2.2$. (For interpretation of the references to color in this figure legend, the reader is referred to the web version of this article.)

Divergence-free basis functions that satisfy all the linear homogeneous boundary conditions were introduced in [9] for two-dimensional flows and were then extended in [10,11] to three-dimensional cases. To make the numerical process clear we briefly describe these bases below. The bases are built from shifted Chebyshev polynomials of the 1st and 2nd kind, $T_n(x)$ and $U_n(x)$, that are defined as

$$T_n(x) = \cos[n \cdot \arccos(2x - 1)], \quad U_n(x) = \frac{\sin[(n+1)\arccos(2x-1)]}{\sin[\arccos(2x-1)]} \quad (13)$$

and are connected via derivative of $T_n(x)$ as $T'_n(x) = 2nU_{n-1}(x)$. Each system of polynomials forms basis in the space of continuous functions defined on the interval $0 \leq x \leq 1$. It is easy to see that vectors

$$\hat{\mathbf{q}}_{ij}^{2D} = \begin{bmatrix} \frac{x}{2i} T_i(\frac{x}{X}) U_{j-1}(\frac{y}{Y}) \\ -\frac{y}{2j} U_{i-1}(\frac{x}{X}) T_j(\frac{y}{Y}) \end{bmatrix} \quad (14)$$

form a divergence-free basis in the space of divergence-free functions defined on a rectangle $0 \leq x \leq X$, $0 \leq y \leq Y$. Assume that a two-dimensional problem is defined with two linear and homogeneous boundary conditions for velocity at each boundary, e.g., the no-slip conditions. This yields four boundary conditions in either

x - or y -direction for the two velocity components. To satisfy the boundary conditions we extend components of the vectors (14) into linear superpositions as

$$\mathbf{q}_{ij}^{2D} = \begin{bmatrix} \frac{x}{2} \sum_{l=0}^4 \frac{a_{il}}{(i+l)} T_{i+l}(\frac{x}{X}) \sum_{m=0}^4 b_{jm} U_{j+m-1}(\frac{y}{Y}) \\ -\frac{y}{2} \sum_{l=0}^4 a_{il} U_{i+l-1}(\frac{x}{X}) \sum_{m=0}^4 \frac{b_{jm}}{(j+m)} T_{j+m}(\frac{y}{Y}) \end{bmatrix} \quad (15)$$

For each i a substitution of (15) into the boundary conditions yields four linear homogeneous equations for five coefficients a_{il} , $l = 0, 1, 2, 3, 4$. Fixing $a_{i0} = 1$, allows one to define all the other coefficients, whose dependence on i and l can be derived analytically. The coefficients b_{jm} are evaluated in the same way. Expressions for these coefficients for the no-slip boundary conditions can be found in [9,11]. Since the basis functions $\hat{\mathbf{q}}_{ij}^{2D}$ are divergence-free in the plane (x, y) , $\partial(\hat{\mathbf{q}}_{ij}^{2D})_x / \partial x + \partial(\hat{\mathbf{q}}_{ij}^{2D})_y / \partial y = 0$, and satisfy the non-penetration conditions through all the boundaries $x = 0, X$ and $y = 0, Y$, they are orthogonal to every two-dimensional potential vector field, i.e.,

$$\int_0^Y \int_0^X \nabla_{2D} p \cdot \mathbf{q}_{ij}^{2D} dx dy = \int_0^Y \int_0^X \left(\frac{\partial p}{\partial x} \mathbf{e}_x + \frac{\partial p}{\partial y} \mathbf{e}_y \right) \cdot \mathbf{q}_{ij}^{2D} dx dy = 0, \quad (16)$$

which is an important point for further evaluations.

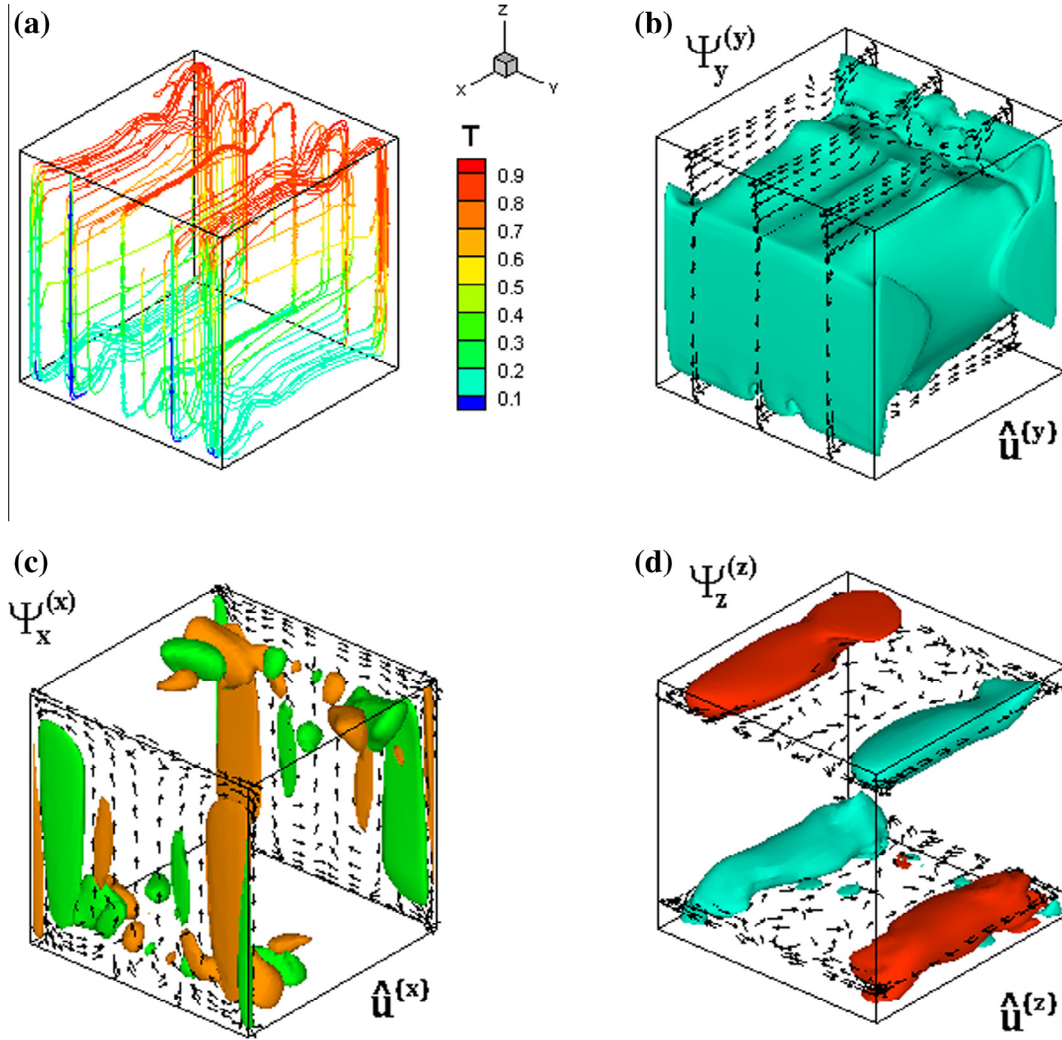


Fig. 6. Visualization of a three-dimensional flow at $Ra = 10^8$. (a) Two flow trajectories starting at the points $(0.1,0.1,0.1)$ $(0.9,0.9,0.9)$ and $(0.1,0.5,0.5)$. The trajectories are colored due to the temperature values at the points they pass. The temperature color map is shown aside. (b), (c), (d) Isosurfaces of Ψ_y , Ψ_x and Ψ_z superimposed with the vector plots of the fields $\mathbf{u}^{(y)}$, $\mathbf{u}^{(x)}$ and $\mathbf{u}^{(z)}$, respectively. The isosurfaces are plotted for $\Psi_y = 39.3$, $\Psi_x = \pm 4.3$, and $\Psi_z = \pm 6.8$. (For interpretation of the references to color in this figure legend, the reader is referred to the web version of this article.)

For extension of the two-dimensional basis to the three dimensional case we recall that for a divergence-free vector field we have to define independent three-dimensional bases for two components only. Representing the flow in the form (5) and using the same idea as in the two-dimensional basis (15) we arrive to a set of three-dimensional basis functions formed from two following subsets

$$\mathbf{q}_{ijk}^{(y)}(x,y,z) = \begin{bmatrix} \frac{x}{2} \sum_{l=0}^4 \frac{\hat{a}_{il}}{(i+l)} T_{i+l}(\frac{x}{\hat{x}}) \sum_{m=0}^4 \hat{b}_{jm} T_{j+m}(\frac{y}{\hat{y}}) \sum_{n=0}^4 \hat{c}_{kn} U_{k+n-1}(\frac{z}{\hat{z}}) \\ 0 \\ -\frac{z}{2} \sum_{l=0}^4 \hat{a}_{il} U_{i+l-1}(\frac{x}{\hat{x}}) \sum_{m=0}^4 \hat{b}_{jm} T_{j+m}(\frac{y}{\hat{y}}) \sum_{n=0}^4 \frac{\hat{c}_{kn}}{(k+n)} T_{k+n}(\frac{z}{\hat{z}}) \end{bmatrix} \quad (17)$$

$$\mathbf{q}_{ijk}^{(x)}(x,y,z) = \begin{bmatrix} 0 \\ \frac{y}{2} \sum_{l=0}^4 \tilde{a}_{il} T_{i+l}(\frac{x}{\hat{x}}) \sum_{m=0}^4 \frac{\tilde{b}_{jm}}{(j+m)} T_{j+m}(\frac{y}{\hat{y}}) \sum_{n=0}^4 \tilde{c}_{kn} U_{k+n-1}(\frac{z}{\hat{z}}) \\ -\frac{z}{2} \sum_{l=0}^4 \tilde{a}_{il} T_{i+l}(\frac{x}{\hat{x}}) \sum_{m=0}^4 \tilde{b}_{jm} U_{j+m-1}(\frac{y}{\hat{y}}) \sum_{n=0}^4 \frac{\tilde{c}_{kn}}{(k+n)} T_{k+n}(\frac{z}{\hat{z}}) \end{bmatrix} \quad (18)$$

where coefficients \hat{a}_{il} , \hat{b}_{jm} , \hat{c}_{kn} , \tilde{a}_{il} , \tilde{b}_{jm} , \tilde{c}_{kn} are defined from the boundary conditions. Their derivation for no-slip boundary conditions is explained in Appendix A. Expressions for these coefficients

in the case of a slip-free condition on the upper boundary can be found in [11]. The velocity field is projected on truncated series

$$\hat{\mathbf{u}}^{(x)} = \sum_{i=0}^{N_x} \sum_{j=0}^{N_y} \sum_{k=0}^{N_z} A_{ijk} \mathbf{q}_{ijk}^{(x)}, \quad \hat{\mathbf{u}}^{(y)} = \sum_{i=0}^{N_x} \sum_{j=0}^{N_y} \sum_{k=0}^{N_z} B_{ijk} \mathbf{q}_{ijk}^{(y)} \quad (19)$$

Here one must be cautious with the boundary conditions in z-direction since, as it was explained above, the two parts of representation (6) satisfy the boundary condition for w at $z=Z$ only as a sum. Therefore we must exclude this condition from definition of basis functions (17) and (18) and set $\hat{c}_{k4} = \tilde{c}_{k4} = 0$. The corresponding boundary condition should be included in the resulting system of equations for A_{ijk} and B_{ijk} as an additional algebraic constraint. Note that this fact was overlooked in [10] that could lead to missing of some important three-dimensional Rayleigh–Bénard modes. On the other hand, comparison of 3D basis functions (17) and (18) with the 2D ones (15) shows that with all the boundary conditions included, the functions $\mathbf{q}_{ijk}^{(y)}(x,y,z)$ and $\mathbf{q}_{ijk}^{(x)}(x,y,z)$ form the complete two-dimensional bases in the $(x,y=const,z)$ and $(x=const,y,z)$ planes, respectively. The coefficients \hat{b}_{jm} and \tilde{a}_{il} are used to satisfy the boundary conditions in the third direction. For the basis in the $(x,y,z=const)$ planes we add

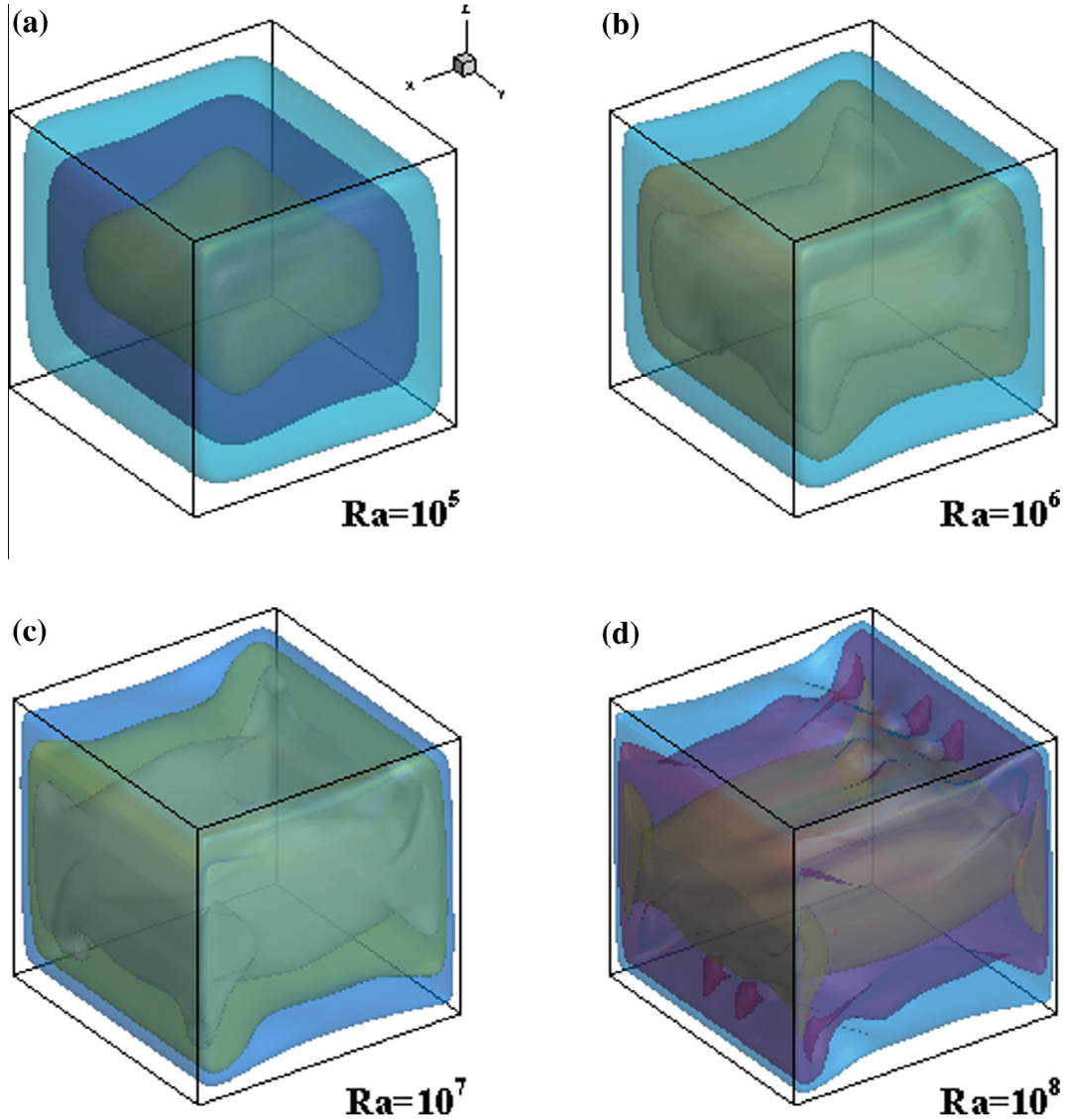


Fig. 7. Isosurfaces of $\Psi_y^{(y)}$ at different Rayleigh numbers. The isosurfaces are plotted at levels (a) 0.53, 4.0, 8.8; (b) 2.5, 10.9, 16.0; (c) 5.4, 17.3, 26.6; (d) 12.6, 33.7, 50.6.

$$\mathbf{q}_{ijk}^{(z)}(x, y, z) = \begin{bmatrix} \frac{x}{2} \sum_{l=0}^4 \frac{\bar{a}_{il}}{(i+l)} T_{i+l}(\frac{x}{\bar{x}}) \sum_{m=0}^4 \bar{b}_{jm} U_{j+m-1}(\frac{y}{\bar{y}}) \sum_{n=0}^4 \bar{c}_{kn} T_{k+n}(\frac{z}{\bar{z}}) \\ -\frac{y}{2} \sum_{l=0}^4 \bar{a}_{il} U_{i+l-1}(\frac{x}{\bar{x}}) \sum_{m=0}^4 \frac{\bar{b}_{jm}}{(j+m)} T_{j+m}(\frac{y}{\bar{y}}) \sum_{n=0}^4 \bar{c}_{kn} T_{k+n}(\frac{z}{\bar{z}}) \\ 0 \end{bmatrix} \quad (20)$$

Together with the third projection of the velocity

$$\hat{\mathbf{u}}^{(z)} = \sum_{i=0}^{N_x} \sum_{j=0}^{N_y} \sum_{k=0}^{N_z} C_{ijk} \mathbf{q}_{ijk}^{(z)} \quad (21)$$

Now, we define an inner product as

$$\langle \mathbf{u}, \mathbf{v} \rangle = \int_V \mathbf{u} \cdot \mathbf{v} dV \quad (22)$$

and compute projections of the velocity vector \mathbf{V} , to be visualized, on each of the three basis systems separately. To do that, we need to calculate Gram matrices G_x, G_y , and G_z for each of the three bases systems $\mathbf{q}^{(x)}$, $\mathbf{q}^{(y)}$, and $\mathbf{q}^{(z)}$, respectively. This does not require much CPU time since inner products in each spatial direction can be calculated separately. The coefficients A_{ijk} , B_{ijk} , and C_{ijk} in the decompositions (19) and (21) are calculated as a product of inversed Gram

matrices with vectors composed of the inner products of the velocity field V with basis functions $\mathbf{q}^{(x)}$, $\mathbf{q}^{(y)}$, and $\mathbf{q}^{(z)}$. The latter can be expressed as

$$\begin{aligned} \{A_{ijk}\} &= G_x^{-1} \left\{ \langle \mathbf{V}, \mathbf{q}_{ijk}^{(x)} \rangle \right\}, & \{B_{ijk}\} &= G_y^{-1} \left\{ \langle \mathbf{V}, \mathbf{q}_{ijk}^{(y)} \rangle \right\}, \\ \{C_{ijk}\} &= G_z^{-1} \left\{ \langle \mathbf{V}, \mathbf{q}_{ijk}^{(z)} \rangle \right\} \end{aligned} \quad (23)$$

where brackets $\{\}$ denote assembling of a 3D array into a vector, which is done by assignment of a single index $l = N_z[N_y(i-1) + j-1] + k$ to each three-dimensional array, e.g., A_{ijk} or $\langle \mathbf{V}, \mathbf{q}_{ijk}^{(x)} \rangle$, described by the indices i, j, k that vary from 1 to N_x, N_y , and N_z , respectively. Adding the definition $J = N_z[N_y(l-1) + m-1] + n$, the (I, J) element of the Gram matrices is defined as $G_x^{(IJ)} = \langle \mathbf{q}_I^{(x)}, \mathbf{q}_J^{(x)} \rangle = \langle \mathbf{q}_{ijk}^{(x)}, \mathbf{q}_{lmn}^{(x)} \rangle$, $G_y^{(IJ)} = \langle \mathbf{q}_I^{(y)}, \mathbf{q}_J^{(y)} \rangle = \langle \mathbf{q}_{ijk}^{(y)}, \mathbf{q}_{lmn}^{(y)} \rangle$, and $G_z^{(IJ)} = \langle \mathbf{q}_I^{(z)}, \mathbf{q}_J^{(z)} \rangle = \langle \mathbf{q}_{ijk}^{(z)}, \mathbf{q}_{lmn}^{(z)} \rangle$. Above integrals must be evaluated numerically using an appropriate quadrature formula. For example, for the finite volume solution defined on staggered grids we used summation of the function values in finite volumes centers multiplied by the corresponding volumes. More details are given in Appendix B. The Gram matrices are symmetric by definition. Their

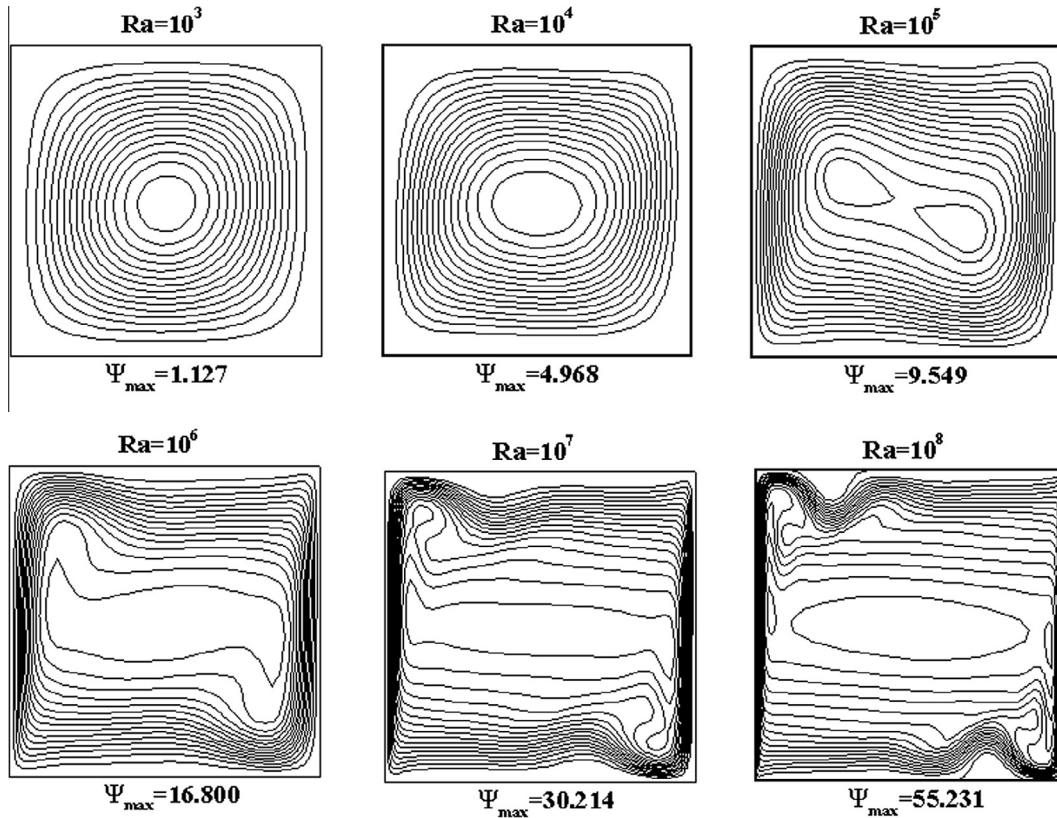


Fig. 8. Isolines of $\Psi_y^{(y)}$ in the midplane $y = 0.5$ at different Rayleigh numbers. The direction of main circulation is clockwise.

inverse is the most CPU time consuming operation for the whole computational process described. For the results described below we used 30 and 40 basis functions in each spatial direction. The obtained results were visually undistinguishable, which is the only type of truncation number independence we need for visualization. The whole computational process was carried out with the double precision arithmetic, and for 30^3 basis functions never consumed more than 20 min for a 2.9 GHz PC. Note, however, that application of the Galerkin method based on above bases for calculation of three-dimensional flows will not be effective because of a very long CPU time needed for evaluation of the non-linear terms.

Since the basis vectors $\mathbf{q}_{ijk}^{(x)}$, $\mathbf{q}_{ijk}^{(y)}$ and $\mathbf{q}_{ijk}^{(z)}$ satisfy all the boundary conditions and are divergence-free not only in the 3D space, but also into the corresponding coordinate planes, the potential parts of projections on these planes are excluded by (16), and resulting vectors $\hat{\mathbf{u}}^{(x)}$, $\hat{\mathbf{u}}^{(y)}$, $\hat{\mathbf{u}}^{(z)}$ satisfy the boundary conditions and are divergence free in the planes where they are located. Therefore, they approximate the quasi-two-dimensional divergence-free projection vectors we are looking for. Note, however, that the superposition $\hat{\mathbf{u}}^{(x)} + \hat{\mathbf{u}}^{(y)} + \hat{\mathbf{u}}^{(z)}$ does not approximate the initial vector \mathbf{v} . To complete the visualization we have to derive the corresponding approximation of vector potentials. The vector potential of each of $\hat{\mathbf{u}}^{(x)}$, $\hat{\mathbf{u}}^{(y)}$, $\hat{\mathbf{u}}^{(z)}$ has only one non-zero component, as is defined below

$$\begin{aligned} \hat{\mathbf{u}}^{(x)} &= \text{rot}[\Psi^{(x)}], \quad \Psi^{(x)} = (\Psi_x^{(x)}, 0, 0), \quad \Psi_x^{(x)} \approx \sum_{i=0}^{N_x} \sum_{j=0}^{N_y} \sum_{k=0}^{N_z} A_{ijk} \varphi_{ijk}^{(x)}, \\ \hat{\mathbf{u}}^{(y)} &= \text{rot}[\Psi^{(y)}], \quad \Psi^{(y)} = (0, \Psi_y^{(y)}, 0), \quad \Psi_y^{(y)} \approx \sum_{i=0}^{N_x} \sum_{j=0}^{N_y} \sum_{k=0}^{N_z} B_{ijk} \varphi_{ijk}^{(y)}, \\ \hat{\mathbf{u}}^{(z)} &= \text{rot}[\Psi^{(z)}], \quad \Psi^{(z)} = (0, 0, \Psi_z^{(z)}), \quad \Psi_z^{(z)} \approx \sum_{i=0}^{N_x} \sum_{j=0}^{N_y} \sum_{k=0}^{N_z} C_{ijk} \varphi_{ijk}^{(z)} \end{aligned} \quad (24)$$

where

$$\begin{aligned} \varphi_{ijk}^{(x)}(x, y, z) &= -\sum_{l=0}^4 \tilde{a}_{il} T_{i+l} \left(\frac{x}{X}\right) \sum_{m=0}^4 \tilde{b}_{jm} T_{j+m} \left(\frac{y}{Y}\right) \sum_{n=0}^4 \tilde{c}_{kn} T_{k+n} \left(\frac{z}{Z}\right) \\ \varphi_{ijk}^{(y)}(x, y, z) &= \sum_{l=0}^4 \frac{\tilde{a}_{il}}{(i+l)} T_{i+l} \left(\frac{x}{X}\right) \sum_{m=0}^4 \tilde{b}_{jm} T_{j+m} \left(\frac{y}{Y}\right) \sum_{n=0}^4 \frac{\tilde{c}_{kn}}{(k+n)} T_{k+n} \left(\frac{z}{Z}\right) \\ \varphi_{ijk}^{(z)}(x, y, z) &= \sum_{l=0}^4 \frac{\tilde{a}_{il}}{(i+l)} T_{i+l} \left(\frac{x}{X}\right) \sum_{m=0}^4 \frac{\tilde{b}_{jm}}{(j+m)} T_{j+m} \left(\frac{y}{Y}\right) \sum_{n=0}^4 \tilde{c}_{kn} T_{k+n} \left(\frac{z}{Z}\right) \end{aligned} \quad (25)$$

As stated above, the vectors $\hat{\mathbf{u}}^{(x)}$, $\hat{\mathbf{u}}^{(y)}$, $\hat{\mathbf{u}}^{(z)}$ are tangent to the isosurfaces of $\Psi_x^{(x)}$, $\Psi_y^{(y)}$ and $\Psi_z^{(z)}$, respectively.

4. Visualization results

We start from the flow at $Ra = 10^3$, that has the simplest pattern (Fig. 3). Fig. 3a shows two trajectories starting at points (0.1, 0.1, 0.1) and (0.9, 0.9, 0.9). The trajectories are colored according to the values of temperature they pass, so that it is clearly seen that the fluid rises near the hot wall and descends near the cold one. Looking only at the trajectories, one can mistakenly conclude that convective circulation weakens toward the center plane $y = 0.5$. Frames 3b–3d show that this impression is misleading. In these frames we plot three vector potentials defined in Eqs. (23), together with the divergence-free velocity projections (shown by arrows) on the corresponding coordinate planes. First, it is clearly seen that the projection vectors are tangent to the isolines of the vector potentials. Then we observe that projections on the $y = \text{const.}$ planes (Fig. 3b) represent the simple convective two-dimensional circulation shown in Fig. 1a. Contrary to the impression of Fig. 3a, the circulations in (x, z) are almost y -independent

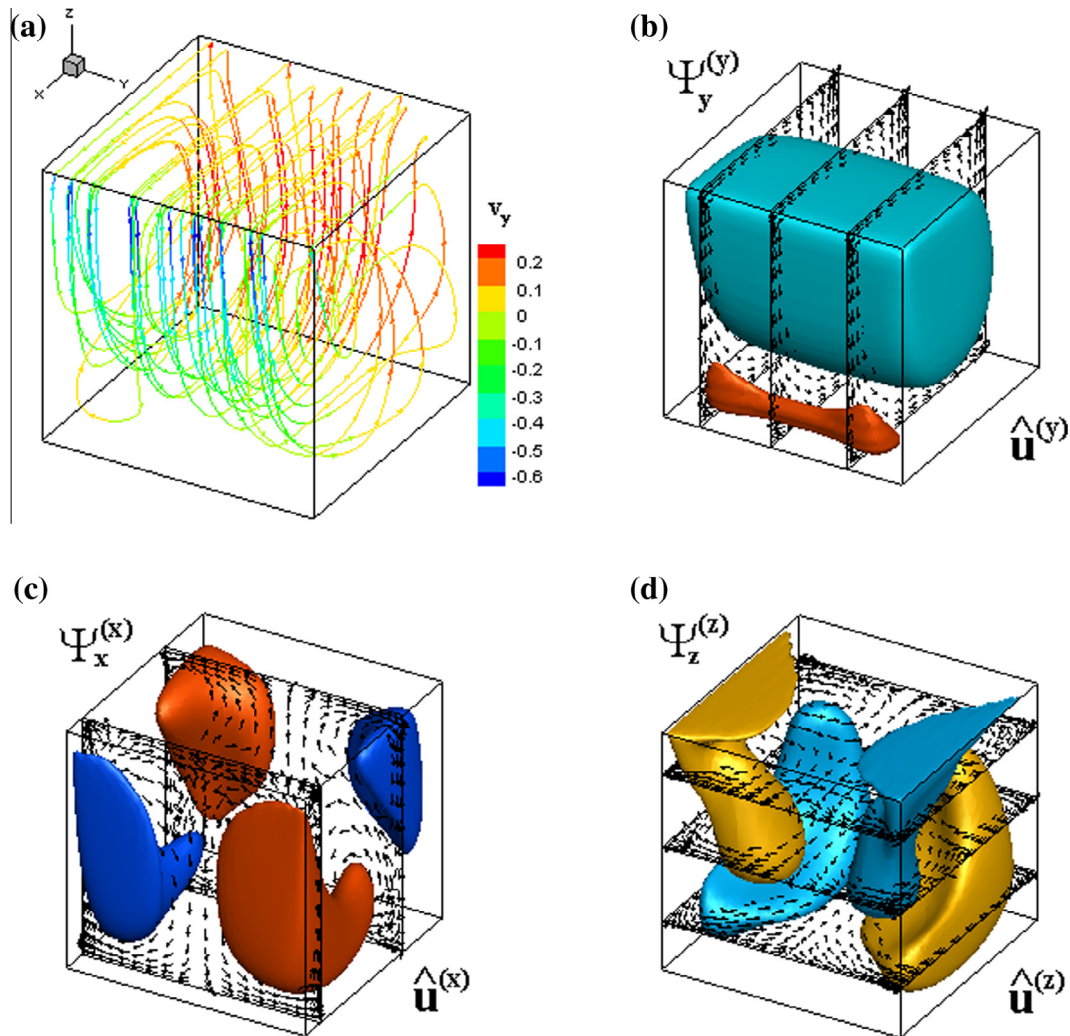


Fig. 9. Visualization of a three-dimensional flow in a lid-driven cubic cavity at $Re = 10^3$. (a) Two flow trajectories starting at the points $(0.4, 0.4, 0.9)$ and $(0.6, 0.6, 0.9)$. The trajectories are colored due to values of spanwise velocity. (b), (c), (d) Isosurfaces of $\Psi_y^{(y)}$, $\Psi_x^{(x)}$ and $\Psi_z^{(z)}$ superimposed with the vector plots of the fields $u^{(y)}$, $u^{(x)}$ and $u^{(z)}$, respectively. The isosurfaces are plotted for $\Psi_y^{(y)} = -0.0032$ and $+0.0008$; $\Psi_x^{(x)} = -0.0044$, and $+0.0033$; $\Psi_z^{(z)} = \pm 0.0028$. (For interpretation of the references to color in this figure legend, the reader is referred to the web version of this article.)

near the center plane $y = 0.5$ and steeply decay near the boundaries $y = 0$ and $y = 1$. The three-dimensional effects are rather clearly seen from the two remaining frames. The flow contains two pairs of diagonally symmetric rolls in the (y, z) planes (Fig. 3c), and two other diagonally symmetric rolls in the (x, y) planes (Fig. 3d). Motion along these rolls deforms trajectories shown in Fig. 3a.

It is intuitively clear that the motion in the frames of Fig. 3 c and d is noticeably weaker than that in Fig. 3b. For the 2D flows the integral intensity of convective circulation can be estimated by the maximal value of the stream function. Similarly, here we can estimate the intensity of motion in two-dimensional planes by maximal values of the corresponding vector potential. Since these values can be used also for comparison of results obtained by different methods we report all of them, together with their locations, in Table 1. As expected, we observe that at $Ra = 10^3$ the maximal value of $\Psi_y^{(y)}$ is larger than that of two other potentials in almost an order of magnitude. With the increase of Rayleigh number the ratio of maximal values of $\Psi_x^{(x)}$, $\Psi_z^{(z)}$ and $\Psi_y^{(y)}$ grows reaching approximately one half at $Ra = 10^7$, which indicates the growing importance of motion in the third direction.

Figs. 4–6 illustrate flows at $Ra = 10^5$, 10^7 and 10^8 , respectively, in the same way as in Fig. 3. It is seen that the isosurfaces of $\Psi_y^{(y)}$ resemble the shapes of two-dimensional streamlines (Fig. 1) rather

closely. At the same time we see that the “three-dimensional additions” to the flow, represented by $\Psi_x^{(x)}$ and $\Psi_z^{(z)}$, remain located near the no-slip boundaries and are weak in the central region of the cavity. This means, in particular, that spanwise directed motion in the midplane $y = 0.5$ is weak, which justifies use of two-dimensional model for description of the main convective circulation.

To show how the isosurfaces of $\Psi_y^{(y)}$ represent patterns of two-dimensional flow we show their several isosurfaces in Fig. 7 and isolines in the center plane $y = 0.5$ in Fig. 8. The isosurfaces of $\Psi_y^{(y)}$ in Fig. 7 show pattern of the main convective circulation in the $(x, y = \text{const}, z)$ planes. The isolines in Fig. 8 can be directly compared with the streamlines shown in Fig. 1. This comparison should be accompanied with the comparison of the maximal values of the stream functions of Fig. 1 and the maximal values of $\Psi_y^{(y)}$, all shown in the figures. We observe that the patterns in Figs. 1 and 8 remain similar, however the similarity diminishes with the increase of Ra . The maximal values of $\Psi_y^{(y)}$ for $Ra \leq 10^5$ are smaller than that of the stream function, which can be easily explained by additional friction losses due to the spanwise boundaries added to the three-dimensional formulation. At $Ra > 10^6$ we observe that together with the deviation of the isolines pattern from the 2D one, the maximal values of $\Psi_y^{(y)}$ become larger than those of the two-dimensional stream function. Ensuring, that this is not an

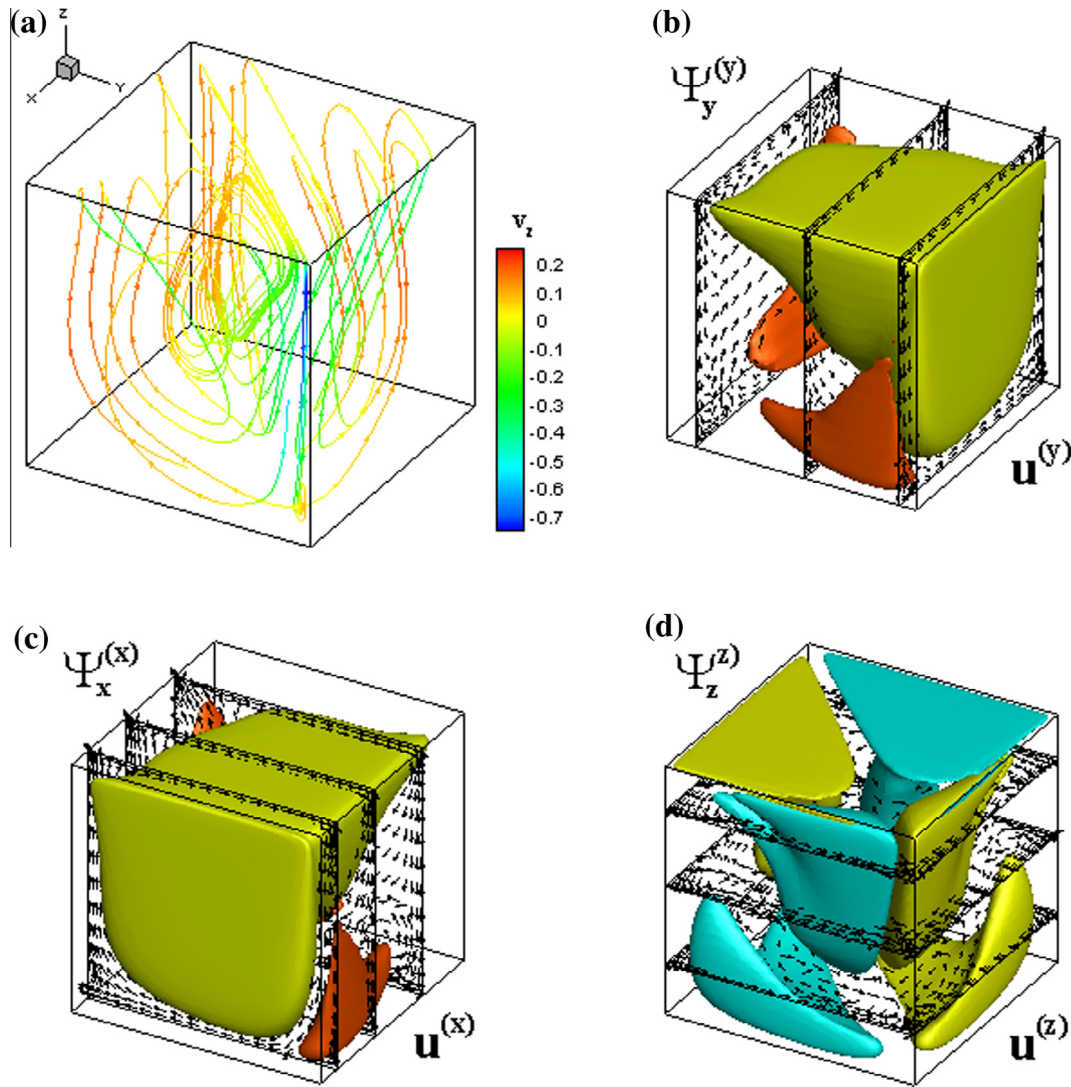


Fig. 10. Visualization of a three-dimensional flow in a lid-driven cubic cavity with a lid moving along a diagonal, at $Re = 10^3$. (a) Two flow trajectories starting at the points $(0.1, 0.1, 0.9)$ and $(0.9, 0.9, 0.9)$. The trajectories are colored due to values of vertical velocity. (b), (c), (d) Isosurfaces of $\Psi_y^{(y)}$, $\Psi_x^{(x)}$ and $\Psi_z^{(z)}$ superimposed with the vector plots of the fields $u^{(y)}$, $u^{(x)}$ and $u^{(z)}$, respectively. The isosurfaces are plotted for $\Psi_y^{(y)} = -0.015$ and $+0.0015$; $\Psi_x^{(x)} = -0.015$, and $+0.0015$; $\Psi_z^{(z)} = \pm 0.0024$. (For interpretation of the references to color in this figure legend, the reader is referred to the web version of this article.)

effect of truncation in the sums (23), we explain this by strong three-dimensional effects, in which motion along the y -axis start to affect the motion in the $(x, y = const, z)$ planes.

As an example of arbitrary choice of projection planes we consider another well-known benchmark problem of flow in a lid-driven cubic cavity. We consider it in two different formulations: a classical configuration where the lid moves parallel to a side wall, and a modified configuration with the lid moving along the diagonal of the upper boundary [12,13]. Obviously, three-dimensional effects are significantly stronger in the second case. Both flows are depicted in Figs. 9 and 10 in the same way as convective flows were represented above. Comparing the flow pattern shown in Fig. 9, one can see clear similarities with the well-known two-dimensional flow in a lid-driven cavity. The main vortex and reverse recirculation in the lower corner are clearly seen in Fig. 9b. Fig. 9c and d show additional three-dimensional recirculations in the $(x, y, z = const)$ and $(x = const, y, z)$ planes. The same representation of the second configuration in Fig. 10 exhibits similar patterns of $\Psi_x^{(x)}$ and $\Psi_y^{(y)}$ together with the similar patterns of corresponding projection vectors. This is an obvious consequence of the problem configuration, where main motion is located in the diagonal plane and the planes parallel to it. To illustrate motion in these

planes we project the flow on planes orthogonal to the diagonal plane (or parallel to the second diagonal plane). The result is shown in Fig. 11. The isosurfaces belong to the corresponding vector potential, so that the divergence-free projection of velocity on the diagonal and parallel planes is tangent to these and other isosurfaces. Arrows in the diagonal plane depict this projection and illustrate the main vortex, as well as small recirculation vortices in lower corners. It is seen that the arrows are tangent to both isosurfaces.

5. Conclusions

We proposed to visualize three-dimensional incompressible flows by divergence-free projections of velocity field on three coordinate planes. We presented the arguments showing that such a representation allows, in particular, for a better understanding of similarities and differences between three-dimensional benchmark flow models and their two-dimensional counter parts. We argued also that the choice of projection planes is arbitrary, so that they can be fitted to the flow pattern.

To approximate the divergence-free projections numerically we calculated orthogonal projections on divergence-free Galerkin velocity bases. Obviously, there are other ways of doing that,

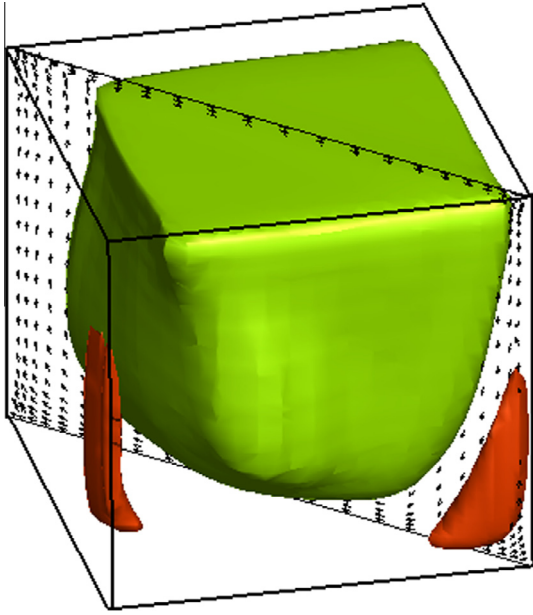


Fig. 11. Visualization of a three-dimensional flow in a lid-driven cubic cavity with a lid moving along a diagonal, at $Re = 10^3$. Isosurfaces of vector potential of velocity projection on the diagonal planes, and the vector plot of the corresponding projected velocity field. The isosurfaces are plotted for the levels -0.017 and $+0.004$, while the minimal and maximal values of the calculated vector potential are -0.083 and $+0.012$.

among which we can mention inverse of the Stokes operator discussed in [14]. We believe also that the proposed method of visualization is suitable for a significantly wider class of incompressible flows, and can be applied not only to numerical, but also to experimental data.

Acknowledgement

This work was supported by the LinkSCEEM-2 project, funded by the European Commission under the 7th Framework Program through Capacities Research Infrastructure, INFRA-2010-1.2.3 Virtual Research Communities, Combination of Collaborative Project and Coordination and Support Actions (CP-CSA) under Grant agreement No. RI-261600.

Appendix A. Derivation of coefficients \hat{a}_{il} , \hat{b}_{jm} , \hat{c}_{kn} , \tilde{a}_{il} , \tilde{b}_{jm} , \tilde{c}_{kn} of the basis functions (17) and (18) for no-slip boundary conditions

As mentioned above, the coefficients \hat{a}_{il} , \hat{b}_{jm} , \hat{c}_{kn} , \tilde{a}_{il} , \tilde{b}_{jm} , \tilde{c}_{kn} are obtained after substitution of the basis functions in the boundary conditions. The values of the shifted Chebyshev polynomials at the boundary points are

$$\begin{aligned} T_n(0) &= (-1)^n, & T_n(1) &= 1, & U_n(0) &= (-1)^n(n+1), \\ U_n(1) &= n+1 \end{aligned} \quad (25)$$

Thus, for the coefficients \hat{a}_{il} we obtain the following system of four linear equations

$$\frac{(-1)^i}{i} \hat{a}_{i,0} + \frac{(-1)^{i+1}}{i+1} \hat{a}_{i,1} + \frac{(-1)^{i+2}}{i+2} \hat{a}_{i,2} + \frac{(-1)^{i+3}}{i+3} \hat{a}_{i,3} + \frac{(-1)^{i+4}}{i+4} \hat{a}_{i,4} = 0 \quad (26.1)$$

$$\frac{1}{i} \hat{a}_{i,0} + \frac{1}{i+1} \hat{a}_{i,1} + \frac{1}{i+2} \hat{a}_{i,2} + \frac{1}{i+3} \hat{a}_{i,3} + \frac{1}{i+4} \hat{a}_{i,4} = 0 \quad (26.2)$$

$$\begin{aligned} (-1)^i(i+1)\hat{a}_{i,0} + (-1)^{i+1}(i+2)\hat{a}_{i,1} + (-1)^{i+2}(i+2)\hat{a}_{i,2} \\ + (-1)^{i+3}(i+4)\hat{a}_{i,3} + (-1)^{i+4}(i+5)\hat{a}_{i,4} = 0 \end{aligned} \quad (26.3)$$

$$(i+1)\hat{a}_{i,0} + (i+2)\hat{a}_{i,1} + (i+2)\hat{a}_{i,2} + (i+4)\hat{a}_{i,3} + (i+5)\hat{a}_{i,4} = 0 \quad (26.4)$$

for five unknown coefficients. To make the system definite, we assign $\hat{a}_{i,0} = 1$, and assuming $i \neq 0$ obtain

$$\begin{aligned} \hat{a}_{i,1} &= \hat{a}_{i,3} = 0, & \hat{a}_{i,2} &= -\frac{i}{i+2} - \frac{(i+1)(i+4)^2}{i(i+2)(i+3)}, \\ \hat{a}_{i,4} &= \frac{(i+1)(i+4)}{i(i+3)} \end{aligned} \quad (27)$$

For the first basis function corresponding to $i=0$ we define additionally $U_{-1}(x) = 0$ and for the zero Chebyshev polynomial replace the coefficient $\hat{a}_{i,0}/i$ by $\hat{a}_{0,0}$. This yields

$$\hat{a}_{0,1} = \hat{a}_{0,3} = 0, \quad \hat{a}_{0,2} = -\frac{16}{3}, \quad \hat{a}_{0,4} = \frac{8}{3} \quad (28)$$

Now we notice that the coefficients \tilde{a}_{il} , \tilde{b}_{jm} , \tilde{c}_{kn} and \tilde{c}_{kn} are obtained from same systems of equations where index i should be replaced by either j or k . Therefore,

$$\begin{aligned} \tilde{a}_{il} &= \tilde{b}_{il} = \tilde{c}_{il} = \tilde{c}_{il} = \hat{a}_{il}; & i &= 0, 1, 2, 3, \dots; \\ l &= 0, 1, 2, 3, 4 \end{aligned} \quad (29)$$

The remaining coefficients \hat{b}_{jm} , \tilde{a}_{il} , and \tilde{c}_{kn} must be defined so that the basis functions vanish on all the boundaries. It is easy to see that

$$\hat{b}_{j,0} = \tilde{a}_{i,0} = \tilde{c}_{k,0} = 1, \quad \hat{b}_{j,2} = \tilde{a}_{i,2} = \tilde{c}_{k,2} = -1 \quad (30)$$

$$\hat{b}_{j,1} = \tilde{a}_{i,1} = \tilde{c}_{k,1} = \hat{b}_{j,3} = \tilde{a}_{i,3} = \tilde{c}_{k,3} = \hat{b}_{j,4} = \tilde{a}_{i,4} = \tilde{c}_{k,4} = 0 \quad (31)$$

Appendix B. Numerical evaluation of divergence free orthogonal projections on a staggered grid

Here we present more details on numerical evaluation of Eqs. (14)–(25) assuming that the flow is calculated on a staggered grid defined in the following way. First, for the grid size $(M_x + 1)(M_y + 1)(M_z + 1)$ we define uniformly distributed grid nodes x_i , y_j , and z_k as

$$x_i = \frac{X}{N_x} i, \quad y_j = \frac{Y}{N_y} j, \quad z_k = \frac{Z}{N_z} k \quad (32)$$

where i, j, k are integers varying from 0 to M_x, M_y, M_z , respectively. The uniformly distributed nodes can be stretched near the boundaries, or redistributed in any other way that does not alter their numbering in the sense $x_0 < x_1 < \dots < x_{M_x}$, etc. To cluster the grid nodes near the boundaries we use the same mapping as in [11]

$$\begin{aligned} x_i &\leftarrow X \left[\frac{x_i}{X} - a \sin\left(2\pi \frac{x_i}{X}\right) \right], & y_j &\leftarrow Y \left[\frac{y_j}{Y} - b \sin\left(2\pi \frac{y_j}{Y}\right) \right], \\ z_k &\leftarrow Z \left[\frac{z_k}{Z} - c \sin\left(2\pi \frac{z_k}{Z}\right) \right] \end{aligned} \quad (33)$$

where a, b , and c can vary from 0 to 0.12. The steepest stretching is obtained for $a = b = c = 0.12$, the values used in the current study. After the stretching is completed we define the shifted nodes

$$\begin{aligned} x_{i+1/2} &= \frac{1}{2}(x_i + x_{i+1}), & y_{j+1/2} &= \frac{1}{2}(y_j + y_{j+1}), \\ z_{k+1/2} &= \frac{1}{2}(z_k + z_{k+1}) \end{aligned} \quad (34)$$

and the corresponding grid steps

$$h_{i+1/2}^{(x)} = x_{i+1} - x_i, \quad h_{j+1/2}^{(y)} = y_{j+1} - y_j, \quad h_{k+1/2}^{(z)} = z_{k+1} - z_k \quad (35)$$

$$\hat{h}_i^{(x)} = x_{i+1/2} - x_{i-1/2}, \quad \hat{h}_j^{(y)} = y_{j+1/2} - y_{j-1/2}, \quad \hat{h}_k^{(z)} = z_{k+1/2} - z_{k-1/2} \quad (36)$$

The numerical solution is obtained on the staggered grids. The scalar variables, i.e., temperature, pressure and velocity divergence, are defined in the nodes (x_i, y_j, z_k) . The x -, y -, and z -velocity components are defined in the nodes $(x_{i+1/2}, y_j, z_k)$, $(x_i, y_{j+1/2}, z_k)$, and $(x_i, y_j, z_{k+1/2})$, respectively. For the following we define the node values of

numerically calculated functions as $p_{ijk}, T_{ijk}, u_{i+1/2,j,k}, v_{i,j+1/2,k}, w_{i,j,k+1/2}$. The velocity divergence is approximated in the nodes (x_i, y_j, z_k) as

$$[div(v)]_{ijk} = \frac{u_{i+1/2,j,k} - u_{i-1/2,j,k}}{\hat{h}_i^{(x)}} + \frac{v_{i,j+1/2,k} - v_{i,j-1/2,k}}{\hat{h}_j^{(y)}} + \frac{w_{i,j,k+1/2} - w_{i,j,k-1/2}}{\hat{h}_k^{(z)}} \quad (37)$$

The finite volume method combined with the fractional step time integration yields zero values of the numerical divergence (37) in the corresponding nodes. To calculate the divergence free projections described above, we prefer to keep these values equal to zero, rather than the exact differential operator div . To do that we define node values of the Chebyshev polynomials of the first kind T

$$T_{n,i}(x_i) = \cos[n \cdot \arccos(2x_i - 1)],$$

$$T_{n,i+1/2}(x_{i+1/2}) = \cos[n \cdot \arccos(2x_{i+1/2} - 1)] \quad (38)$$

The node values of second kind polynomial U are defined in the way that makes the numerical approximation of the relation $T'_n(x) = 2nU_{n-1}(x)$ valid. Therefore, in all the inner points we define

$$U_{n-1,i}(x_i) = \frac{1}{2nh_i^{(x)}} [T_{n,i+1/2}(x_{i+1/2}) - T_{n,i-1/2}(x_{i-1/2})] \quad (39.1)$$

$$U_{n-1,i+1/2}(x_{i+1/2}) = \frac{1}{2nh_{i+1/2}^{(x)}} [T_{n,i+1}(x_{i+1}) - T_{n,i}(x_i)] \quad (39.2)$$

and add the analytical values of U_n in all the boundary points. The polynomials grid values in the y - and z -direction are defined in the same way. After the polynomials in Eqs. (14)–(20) are replaced by their grid values, the approximate divergence (37) of the basis functions remains an analytic zero. Since boundary values of the grid-defined polynomials are the same as those of the analytical ones, the coefficients found as described in Appendix A remain unchanged. Clearly, redefinition of the polynomials U (39) is not necessary for the visualization purposes, however it yields better comparison with the two-dimensional results that were calculated keeping the 2D version of the divergence approximation (37) equal to zero.

Now, the inner product of two vectors $\mathbf{u} = (u^{(x)}, u^{(y)}, u^{(z)})$ and $\mathbf{w} = (w^{(x)}, w^{(y)}, w^{(z)})$ defined by Eq. (22) is replaced by the following quadrature formula

$$\langle \mathbf{u}, \mathbf{w} \rangle = \sum_{i=1}^{M_x-2} \sum_{j=1}^{M_y-2} \sum_{k=1}^{M_z-2} \left[u_{i+1/2,j,k}^{(x)} w_{i+1/2,j,k}^{(x)} \hat{h}_i^{(x)} \hat{h}_j^{(y)} \hat{h}_k^{(z)} \right] + \sum_{i=1}^{M_x-1} \sum_{j=1}^{M_y-2} \sum_{k=1}^{M_z-2} \left[u_{i,j+1/2,k}^{(y)} w_{i,j+1/2,k}^{(y)} \hat{h}_i^{(x)} \hat{h}_j^{(y)} \hat{h}_k^{(z)} \right] + \sum_{i=1}^{M_x-1} \sum_{j=1}^{M_y-1} \sum_{k=1}^{M_z-2} \left[u_{i,j,k+1/2}^{(z)} w_{i,j,k+1/2}^{(z)} \hat{h}_i^{(x)} \hat{h}_j^{(y)} \hat{h}_k^{(z)} \right] \quad (40)$$

The Gram matrices and the inner products of Eqs. (23) are computed using the quadrature (40). Since the Gram matrices are symmetric and positive defined, they can be effectively inverted by the Cholesky decomposition.

The characteristic CPU times needed for computing of the Gram matrices, their inverse and further summation of the series (24) are shown in Table 2. The last row of Table 2 displays the maximal

Table 2

CPU times consumed using 2.9 GHz PC for computation of the Gram matrices, solution of the linear algebraic equations problem with a Gram matrix by the Cholesky decomposition and computation of the final sums.

Number of basis functions	Computing a single Gram matrix (s)	Solution of a linear problem with a Gram matrix (s)	Calculations of sums (24) (s)	Absolute error in solution of the linear system
20 ³	0.895	10.6	0.099	1.4 × 10 ⁻¹⁶
30 ³	9.0	380	0.17	4.6 × 10 ⁻¹⁶
40 ³	61.8	5700	0.286	5.0 × 10 ⁻¹⁶

absolute residual over all rows of the linear equations systems, which shows that no numerical difficulties connected to a possible ill-conditioning of the linear systems are observed. Clearly, the most computationally demanding is the Gram matrix inverse. It should be stressed, however, that these matrices depend only on the geometry and boundary conditions, so that they can be calculated once for a series of visualizations, say, at different Reynolds or Grashof numbers. For visualization purposes we usually do not need too demanding convergence. Thus, in the present study the results obtained with 30³ and 40³ basis functions, were visually indistinguishable.

References

- [1] McLaughlin T, Laramée RS, Peikert R, Post FH, Chen M. Over two decades of integration-based, geometric flow visualization. *Comp Graph Forum* 2010;29:1807–29.
- [2] Edmunds M, Laramée RS, Chen G, Max N, Zhang E, Ware C. Surface-based flow visualization. *Comp Graph* 2012;36:974–90.
- [3] Etien T, Nguyen H, Kirby RM, Siva CT. “Flow visualization” juxtaposed with “visualization of flow”: synergistic opportunities between two communities. In: Proceedings of the 51st AIAA aerospace science meeting. New Horiz. Forum Aerosp. Exp.; 2013. p. 1–13.
- [4] Le Quéré P. Accurate solutions to the square thermally driven cavity at high Rayleigh number. *Comp Fluids* 1991;20:29–41.
- [5] Tric E, Labrosse G, Betrouni M. A first incursion into the 3D structure of natural convection of air in a differentially heated cavity, from accurate numerical solutions. *Int J Heat Mass Transf* 1999;43:4043–56.
- [6] Wakashima S, Saitoh TS. Benchmark solutions for natural convection in a cubic cavity using the high-order time-space method. *Int J Heat Mass Transf* 2004;47:853–64.
- [7] Gelfgat AYU. Stability of convective flows in cavities: solution of benchmark problems by a low-order finite volume method. *Int J Numer Meths Fluids* 2007;53:485–506.
- [8] Foias C, Manley O, Rosa R, Temam R. Navier–Stokes equations and turbulence. Cambridge Univ. Press; 2001.
- [9] Gelfgat AYU, Tanasawa I. Numerical analysis of oscillatory instability of buoyancy convection with the Galerkin spectral method. *Numer Heat Transf. Pt A* 1994;25(6):627–48.
- [10] Gelfgat AYU. Different modes of Rayleigh–Bénard instability in two- and three-dimensional rectangular enclosures. *J Comput Phys* 1999;156:300–24.
- [11] Gelfgat AYU. Two- and three-dimensional instabilities of confined flows: numerical study by a global Galerkin method. *Comput Fluid Dynam J* 2001;9:437–48.
- [12] Povitsky A. Three-dimensional flow in cavity at Yaw. *J Nonlin Anal* 2005;63:e1573–84.
- [13] Feldman Yu, Gelfgat AYU. From multi- to single-grid CFD on massively parallel computers: numerical experiments on lid-driven flow in a cube using pressure-velocity coupled formulation. *Comp Fluids* 2011;46:218–23.
- [14] Vitoshkin H, Gelfgat AYU. On direct inverse of Stokes, Helmholtz and Laplacian operators in view of time-stepper-based Newton and Arnoldi solvers in incompressible CFD. *Commun Comput Phys* 2013;14:1103–19.